HHS Public Access

Author manuscript

Nat Mater. Author manuscript; available in PMC 2023 August 09.

Published in final edited form as:

Nat Mater. 2023 February ; 22(2): 249–259. doi:10.1038/s41563-022-01396-x.

Active tissue adhesive activates mechanosensors and prevents muscle atrophy

Sungmin Nam[1,2], **Bo Ri Seo**[1,2], **Alexander J. Najibi**[1,2], **Stephanie L. McNamara**[1,2], **David J. Mooney**[1,2,*]

[1]John A. Paulson School of Engineering and Applied Sciences, Harvard University, Cambridge, MA 02138, USA.

[2]Wyss Institute for Biologically Inspired Engineering, Harvard University, Boston, MA 02115, USA

Abstract

While mechanical stimulation is known to regulate a wide range of biological processes at the cellular and tissue level, its medical use for tissue regeneration and rehabilitation has been limited by the availability of suitable devices. Here we present a mechanically active gel-elastomer-nitinol tissue adhesive (MAGENTA) that generates and delivers muscle contraction mimicking stimulation to a target tissue with programmed strength and frequency. MAGENTA consists of a shape memory alloy spring that enables actuation up to 40% strain, and an adhesive that efficiently transmits the actuation to the underlying tissue. MAGENTA activates mechanosensing pathways involving yes-associated protein (YAP) and myocardin related transcription factor A (MRTFA) and increases the rate of muscle protein synthesis. Disuse muscles treated with MAGENTA exhibit greater size and weight, and generate higher forces compared to untreated muscles, demonstrating prevention of atrophy. MAGENTA has thus promising applications in the treatment of muscle atrophy and regenerative medicine.

Mechanical tissue stimulation is attractive to promote tissue regeneration and rehabilitation, as it can provide localized activity, may avoid pleiotropic effects, and also lead to a simplified regulatory approval process, as compared to traditional drug therapies. Cells and tissues can respond to microenvironmental biophysical cues and external mechanical stimuli through a process termed mechanotransduction, which converts physical signals into changes in cell function[1,2]. Studies investigating the impact of mechanical stimulation on cells and engineered tissue constructs have found that mechanical stimuli (e.g., stretching) can regulate cell proliferation[3-5], force generation[6,7], and cell differentiation[8]. Further, mechanical devices are routinely used in clinical procedures such as distraction osteogenesis[9], tissue expansion[10], and orthodontics[11]. Recent preclinical studies have demonstrated the therapeutic effect of compressive loading (e.g., mechanotherapy) on

*Corresponding author. mooneyd@seas.harvard.edu.

Author contributions

S.N., B.R.S. and D.J.M. conceived the study and designed the experiments. S.N., B.R.S., A.J.N., and S.L.M. carried out the experiments. S.N. performed computational simulations. S.N. and D.J.M. wrote the manuscript.

Competing interests

S.N. and D.J.M. are inventors on patent applications on the active adhesives utilized in this study (U.S. Patent Application No. 63/299,433).

muscle regeneration and rehabilitation[12-15]. However, it remains largely unknown whether externally imposed stretching or contraction can also lead to such beneficial effects.

There are two major technical challenges to mechanically stimulate tissues in vivo through stretching or contraction; one is the development of a mechanical system capable of generating forces or strains along the tissue surface, and the other is the formation of a robust tissue interface that can effectively deliver these stimuli to the tissue. While the field of soft robotics has advanced a variety of mechanisms to generate mechanical actuation[16,17], many are neither biocompatible nor applicable to the body, limiting their use for biomedical applications. One promising candidate is shape memory alloys (SMAs), which have been widely used in medical devices due to their robust mechanical properties, high resiliency and biocompatibility[18]. Springs fabricated from SMAs can generate mechanical forces and actuations in a controlled manner using relatively low voltages, suggesting them to be suitable for biocompatible soft robotic actuators[18,19]. In parallel, a class of tissue adhesives based on tough hydrogels can achieve strong adhesion with many tissue types[20,21]. These hydrogels have also been shown to integrate with engineered materials such as elastomers[22,23]. Combining these two types of materials may provide biomedical devices that enable mechanical stretching or contraction of the target tissue.

One potential therapeutic target for mechanical stimulation devices is muscle atrophy. Muscle atrophy results from physical inactivity or denervation, and also occurs as a systematic response to fasting and various diseases, including cancer associated cachexia and diabetes[24-26]. During the progression of atrophy, muscle mass is lost due to the accelerated degradation of myofibrillar and soluble proteins and the decreased synthesis of new proteins, resulting in weakened muscle and increased disability[24]. While muscle atrophy can be prevented or slowed through exercise[27], this is often not feasible (e.g., patients under bed rest). Therefore, effective countermeasures to muscle atrophy still often represent an unmet clinical need, and delivery of mechanical stimulation could be an alternative and complimentary treatment. While mechanotherapy (e.g., massage therapy) has been proposed to alleviate muscle atrophy[13,28], the impact of mechanical stretching or contraction has not been explored.

Here we develop a mechanically active gel-elastomer-nitinol tissue adhesive (MAGENTA) that can robustly adhere to skeletal muscle and deliver a stimulation that mimics muscle contraction with desired strength and frequency (Fig. 1a). The mechanical actuation of MAGENTA is enabled by a soft robotic actuator made of a shape memory alloy (i.e., nitinol) spring and an elastomer. Tissue adhesion is achieved by incorporating a hydrogel-based adhesive, which interfaces the underlying tissue and transmits the actuation, providing mechanical stimulation in a localized and controlled manner. Interestingly, this mechanical stimulation was found to attenuate muscle atrophy as well as promote recovery from atrophy. While this study is mainly focused on using electric voltage to generate the actuation of MAGENTA, we further demonstrate that MAGENTA can also be actuated by laser irradiation, suggesting the possibility of remote control.

Design and mechanism of the soft actuator

To implement MAGENTA, we first developed a soft robotic actuator using a nitinol spring and an elastomer to ensheathe the spring (Fig. 1b). While the spring enables mechanical actuation, the elastomer forms the body of the actuator, providing structural and mechanical support. To fabricate the actuator, the nitinol spring was connected to electric wires, and embedded in an elastomer (Supplementary Fig. 1a, see Methods for the detailed fabrication process). When voltage was applied, the actuator rapidly contracted until the force balance between spring contraction and elastomer resistance was achieved (Supplementary Fig. 1b; Supplementary Video 1). The actuation strain, defined as the ratio of the change in spring length to the initial length, was controlled in a voltage-dependent manner to the maximum value (Figure 1c and d). When the current was discontinued, the contracted actuator relaxed promptly to its initial state, driven by the restoring force of the elastomer, allowing for consecutive actuation (Fig. 1c). The frequency and duration of actuation can be simply programmed through a microprocessor (Supplementary Fig. 1c). Given the simplicity of the fabrication process, the design and size of the actuators can be readily scaled from millimeters to several centimeters (Supplementary Fig. 1d). This approach established a simple yet facile method to build soft robotic actuators that can provide programmed actuation on demand.

Since the actuation strain is determined by the force balance between the spring and the elastomer (Fig. 2a), the role of elastomer stiffness in regulating actuation strain was next examined. Elastomers with different formulations were prepared to adjust the stiffness of the elastomer (Fig. 2b and Supplementary Fig. 2a). Under the same voltage, increasing the stiffness of the elastomer was found to decrease the actuation strain (Fig. 2c). In contrast, the actuation force, measured as the force transmitted to the underlying substrate, increased with the stiffness of the elastomer (Fig. 2c and Supplementary Fig. 2b). This inverse correlation of force and strain with respect to stiffness is attributed to the constant total energy provided by the electric voltage.

In addition, we also characterized the thermal performance of actuators by visualizing the temperature in real-time using a thermographic camera. When voltage was applied, the temperature of the actuator peaked at the center location of the spring, and decreased rapidly from the center. This resulted in a temperature difference of 15°C between the center and surface (Fig. 2d; Supplementary Fig. 3a). During cyclic actuation, the temperature averaged along the actuator surface increased during the first few cycles of actuation and then reached a plateau as thermal accumulation and dissipation entered a steady state (Fig. 2e; Supplementary Fig. 3b). As the frequency increased, the rate of thermal accumulation was initially greater than that of dissipation, resulting in a higher maximum temperature regardless of the elastomer stiffness (Fig. 2f; Supplementary Fig. 3b). In contrast, at a constant frequency, the temperature decreased with increasing stiffness of the elastomer (Fig. 2f). The relationship between temperature increase and actuation frequency was similar at both ambient or body temperature (37°C) (Fig. 2g; Supplementary Fig. 3c).

Prediction of tissue deformation

To determine which combination of mechanical parameters of elastomers and tough hydrogels could enable maximum tissue deformation, computational simulations were performed (Fig. 2h; Supplementary Fig. 4, a-c). The tissue stiffness was set to 10 kPa, as determined through measurements of skeletal muscle (Supplementary Fig. 4d). The tissue strain was found to have a biphasic dependence on the elastomer stiffness, with the maximum strain generated at a stiffness of ~130 kPa (Fig. 2i; Supplementary Fig. 4e). A similar trend was found for all adhesive gel stiffness values, indicating that an elastomer stiffness of ~130 kPa produced the maximum tissue deformation. The role of gel stiffness and thickness on tissue strain was next explored. A biphasic relationship between tissue strain and gel stiffness was found, with highest tissue strains at medium values of gel stiffness (30 – 60 kPa), independently of gel thickness (Fig. 2j; Supplementary Fig. 4f). Tissue deformation decreased as gel thickness increased (Fig. 2j), and varying the adhesive stiffness within the optimal range had minimal impact on this trend (Fig. 2k). Based on these results, an elastomer of ~130 kPa and an adhesive gel of 30 – 60 kPa with a minimum thickness are desired.

Assembly and functional characterization of MAGENTA

The actuator-adhesive hybrid was prepared by chemically anchoring the elastomer component of the actuator to the hydrogel adhesive (Fig. 3a). As the adhesive matrix will undergo cyclic deformation during actuation, cyclic compression tests were performed to determine its impact. The stiffness of the hydrogels declined during the first few compressions and stabilized over the next hundreds of compressions (Fig. 3b). We defined the stiffness of the hydrogels as the average value over 500 cyclic tests. On the basis of the simulation results, the chemical and physical crosslinking density of the gels was tuned such that the stiffness value was in the range of 30 – 60 kPa (Fig. 3c), which was predicted to generate the maximum tissue strain (Fig. 2j). The hydrogel was then chemically bonded to the elastomer of the actuator using benzophenone[23]. The other face of the hydrogel was anchored to tissue with a chitosan bridging polymer (see Methods). The actuator-hydrogel hybrid with tissue adhesion is hereafter referred to as the mechanically active gel-elastomer-nitinol tissue adhesive (MAGENTA). T-peel tests confirmed a robust assembly of the elastomers, hydrogels, and tissues, with interfacial toughness of the elastomer-hydrogel and hydrogel-tissue interface measured to be above 800 Jm^{-2} and 600 Jm^{-2}, respectively (Fig. 3d-f; Supplementary Video 2 and 3).

In vitro, ex vivo, and in vivo application of MAGENTA

To demonstrate the ability of MAGENTA to deliver therapeutic mechanical stimulation, MAGENTA was first applied to a phantom hydrogel tissue (Fig. 3g; Supplementary Fig. 5a-c). Upon applying voltage, the MAGENTA contracted, and the underlying phantom tissue was deformed accordingly (Supplementary Fig. 5a-c; Supplementary Video 4 and 5). MAGENTA was next applied to skeletal muscle tissue ex vivo. The MAGENTA contraction again led to the deformation of the underlying tissue (Fig. 3h; Supplementary Fig. 5d; Supplementary Video 6), and the experimentally measured tissue strain was similar

to that predicted by the simulation (Fig. 2h-k and Fig. 3i; Supplementary Fig. 4e and f). Some degree of tissue strain along the axis perpendicular to the actuation axis was also observed, due to the outward expansion of the tissue as it was displaced towards the center along the parallel axis. Actuation over multiple cycles confirmed that the MAGENTA continuously and repeatedly deformed the underlying tissue without substantial hysteresis while maintaining its tissue adhesion (Supplementary Fig. 6; Supplementary Fig. 7; Supplementary Video 7).

To assess the in vivo delivery of mechanical stimulation, MAGENTA was implanted on the lateral gastrocnemius in mice (Supplementary Fig. 8). The skin surrounding MAGENTA was displaced upon actuation of the MAGENTA (Fig. 3j; Supplementary Video 8). Real-time high resolution ultrasound imaging confirmed that the skeletal muscle underlying the MAGENTA was substantially deformed along the actuation axis during actuation (Fig. 3k and l; Supplementary Video 9). Although the magnitude of tissue displacement decreased with increasing tissue depth, displacement was still observed at a tissue depth of ~2/3 of the muscle thickness (Fig. 3m).

The biological compatibility of MAGENTA was initially analyzed by co-culturing with C2C12 myoblasts. No significant decrease in cell viability was found with MAGENTA exposure (Supplementary Fig. 9a and b). MAGENTA was subsequently implanted into mice, and histological assessment demonstrated minimal to mild inflammation (Supplementary Fig. 9c and d). Next, the impact of stimulation on biocompatibility was assessed. MAGENTA was applied to muscles of healthy mice, and mechanical stimulation was performed. Similar to the muscles treated with MAGENTA alone, stimulated muscles also showed only minimal to mild inflammation, and no significant effects were observed on tissue homeostasis, including cell proliferation and vascularization (Supplementary Fig. 10).

The effect of MAGENTA-mediated stimulation on biological processes was then evaluated in vitro. First, gelatin and collagen-based hydrogels were prepared as culture substrates that can tolerate repeated mechanical deformation by MAGENTA. C2C12 cells were then placed on the gels, and mechanical stimulation was performed through MAGENTA (Supplementary Fig. 11a) to mimic MAGENTA-treated muscle tissues in vivo. Mechanical stimulation by MAGENTA significantly increased the proliferation of C2C12 cells, and also enhanced their fusion (Supplementary Fig. 11, b-e).

Physiological impact of MAGENTA on muscle atrophy

Next, we investigated whether mechanical stimulation generated by MAGENTA and delivered to the underlying muscle tissue could prevent loss of function in a model of disuse muscle atrophy (Fig. 4a). MAGENTA was adhered on gastrocnemius muscle to generate motion mimicking muscle stretching and contraction. First, the ability of mechanical stimulation to upregulate mechanotransduction pathways in skeletal muscle was assessed by analyzing YAP expression and localization[29,30]. Mice treated with stimulation for two weeks while the limb was immobilized exhibited significantly higher expression levels and nuclear localization of YAP compared to those untreated (Fig. 4b, c and f). Mechanical stimulation also upregulated the protein expression level of MRTFA and increased its

nuclear localization (Fig. 4d, e, and g). Spatial distribution analysis of YAP and MRTFA revealed that their activation was relatively uniformly distributed throughout the muscle, although slight variations from location to location were observed (Supplementary Figs. 12, 13, and 14).

To determine whether mechanical stimulation could affect muscle protein synthesis, newly synthesized protein was quantified through acute incorporation of puromycin. Stimulated muscles exhibited greater puromycin incorporation compared to untreated muscles (Fig. 4h). Immunoblot analysis for MuRF1, a critical regulator that facilitates the degradation of myosin heavy chain (MHC) and accelerates the process of disuse atrophy[31], showed that stimulated muscles displayed reduced MuRF1 expression (Fig. 4i). In addition, the protein expression of Akt and its activated form, phosphorylated Akt, known to be involved in protein synthesis and alleviation of muscle atrophy[26,32], were significantly upregulated in stimulated muscles (Supplementary Fig. 15a). Furthermore, the level of insulin like growth factor-1 (IGF-1), a key determinant of protein synthesis along with Akt[33,34], was also increased in stimulated muscles (Supplementary Fig. 15b).

After confirming the impact of stimulation by MAGENTA at the protein and cellular level, the physiological outcomes were analyzed. Histological analysis and immunohistochemical staining for laminin, MHC, and desmin showed that mice treated with stimulation had muscle fibers with larger cross-sectional area and greater levels of MHC and desmin expression, as compared to untreated mice (Fig. 5, a-c; Supplementary Fig. 15, c-e). The fractions of cells positive for Ki67 and Pax7, indicative of proliferating cells and satellite stem cells, were also higher with mechanical stimulation (Supplementary Fig. 15, f-i). In addition, the gross size and weight of muscles were measured greater in stimulated mice (Fig. 5d and e). However, no significant increase was observed in matrix protein deposition (Supplementary Fig. 16). All sets of mice had similar body weight after 2 weeks (Fig. 5f). Muscle function analysis demonstrated that the muscles of treated mice generated substantially higher tetanic forces than those of untreated mice, with force levels similar to those of muscles in healthy, active mice (Fig. 5g and h).

To gain further insight into the therapeutic effect of MAGENTA, various settings of disuse muscle atrophy were explored. We first examined the impact of duration of mechanical stimulation. Mice were immobilized for 2 weeks, during which mechanical stimulation was performed only in the first week (Supplementary Fig. 17a). Compared to the muscles treated with 2 weeks of stimulation, those treated for only the first week exhibited smaller muscle weight and generated reduced tetanic forces (Supplementary Fig. 17, b-d). Next, we examined MAGENTA efficacy across 3 weeks of immobilization and stimulation. Similar to the 2-week experiment, the stimulation group showed greater muscle weight and tetanic force generation than the control group (Supplementary Fig. 18). However, despite mechanical stimulation, both muscle weight and tetanic force generation of mice at 3 weeks were trending lower than those at 2 weeks.

The potential benefits of mechanical stimulation for functional recovery from disuse atrophy were also analyzed. For this experiment, mice were first atrophied for 3 weeks (Supplementary Fig. 19a), and then mechanical stimulation was performed for

the subsequent week. Similar to the prevention experiments, mechanically stimulated muscles displayed greater weight and tetanic force generation compared to those untreated (Supplementary Fig. 19, b-f).

To compare MAGENTA with another form of mechanical stimulation, we tested whether compressive stimulation through a non-invasive skin interface could also lead a therapeutic effect on disuse muscles (Supplementary Fig. 20a). A previously established robotic system was used to apply controlled and quantifiable compression forces[15] (Supplementary Fig. 20b). Similar to the prevention experiments with MAGENTA, muscle atrophy was induced through hindlimb immobilization for two weeks, and mice were treated with compressive stimulation using the robotic device (Supplementary Fig. 20c). Interestingly, we did not find any significant improvement in muscle weight and force generation in muscles treated with compressive stimulation, as compared to untreated muscles (Supplementary Fig. 20, d-f).

Remote control of MAGENTA

Having established the performance and therapeutic potential of MAGENTA driven by electric signals, we finally explored the possibility of remote control of MAGENTA (Fig. 6a). Hyperspectral imaging showed that the nitinol spring exhibited very low reflectivity at all wavelengths in the range of 420 – 1000 nm (Supplementary Fig. 21a and b), indicating that the spring could absorb light to actuate. To test this hypothesis, a wireless nitinol actuator was first laser-irradiated. Thermography confirmed that the temperature of the actuator rapidly increased in a manner dependent on the distance between the laser and the actuator (Fig. 6b and c; Supplementary Fig. 21c). Importantly, laser irradiation led to contraction of the actuator (Fig. 6d; Supplementary Fig. 21d and e; Supplementary Video 10). The light responsive actuator was then used to create a wireless, remote-controllable MAGENTA (Supplementary Fig. 21f). Ex vivo experiments demonstrated, similar to the electric MAGENTA, that actuation of wireless MAGENTA deformed the underlying muscle tissue along the actuator axis (Fig. 6e and f). After implantation, the wireless MAGENTA was observed to contract following laser irradiation through the mouse skin (Fig. 6g; Supplementary Video 11), demonstrating the remote delivery of mechanical stimulation. In addition, the responsiveness of MAGENTA versus implantation depth was evaluated. The wireless MAGENTA was first adhered to excised muscle tissues, and porcine skin and muscle tissues were then placed on top of the MAGENTA to simulate varying implantation depth (Supplementary Figure 22, insets). Laser irradiation through ~1 mm thick porcine skin and ~2 mm thick mouse muscle tissue successfully led to contraction of MAGENTA, resulting in deformation of the underlying tissue (Supplementary Figure 22, a and c; Supplementary Video 12 and 13). However, ~1.5 mm thick porcine skin including the subcutaneous fat layer did not allow for the MAGENTA to actuate (Supplementary Figure 22b), likely due to laser light absorption as it passed through the fat layer[35].

Outlook

This study developed MAGENTA, a biomedical device capable of adhering to a target tissue and delivering muscle-contraction-mimicking mechanical stimuli in a controlled manner to promote tissue regeneration and rehabilitation. The actuation of MAGENTA, driven by

nitinol spring contraction, led to tissue displacement not only on the tissue surface but also inside the tissue. The therapeutic effects of MAGENTA were demonstrated in a disuse muscle atrophy model. With mechanical stimulation, the occurrence of atrophy was delayed, and recovery was facilitated. While the current work focused on skeletal muscle stimulation in the context of disuse atrophy, this system may also be directly applicable to other types of tissues, including skin and heart (Supplementary Fig. 23). Finally, to broaden the potential use of MAGENTA in a variety of medical settings, we demonstrated its wireless, remote-controlled actuation with a laser.

The ability of MAGENTA to enable mechanical stimulation through tissue stretching/contraction contrasts with previous stimulation systems that provide compressive loading. Many soft robotic systems have been developed to apply mechanical compression for therapeutic purposes through magnetic[12,36], dielectric[37], motor[15,38], and pneumatic[39-41]-based forces. However, fewer efforts have been made to enable tissue stretching or contraction[10,42]. Liquid crystal elastomers (LCEs) can be used as active stretching/contraction mechanisms in vivo. However, their operating temperatures are typically well above the physiological range[16,43,44], and the cytotoxicity of residual monomers resulting from LCE synthesis can raise concerns about biocompatibility[45]. Alternatively, our SMA-based actuators provide a simple and versatile approach to implementing tissue stretching/contraction with a biocompatible actuation mechanism and scalable design. The therapeutic efficacy of stretching/contraction stimulation by MAGENTA was compared with compressive stimulation. Interestingly, compressive stimulation through a non-invasive skin interface did not lead to any significant improvement of muscle weight and force generation in atrophying muscles. This highlights the effectiveness of MAGENTA despite the required implantation procedure. While one set of parameters for compressive stimulation was used in this study, other optimized parameters could yield therapeutic efficacy.

While remote control systems typically involve complex electrical circuits, such as near field communication (NFC)[46-48] and radio frequency (RF) system[49,50], and require a large physical space to mount these additional equipment, wireless actuation of MAGENTA is possible without additional electric components or complex application systems. This was enabled by the light absorption of SMA and consequent thermal generation. The laser-driven actuation of SMA has not been previously studied. However, compared to the electric MAGENTA, wireless MAGENTA has a limited actuation frequency due to the time of thermal generation required with laser irradiation. In addition, since the laser intensity decreases with tissue depth, wireless MAGENTA cannot currently be implanted deep into the body. Future work on surface modification of wireless MAGENTA to increase its light sensitivity could address these limitations and improve the device’s performance.

Methods

Fabrication of soft actuator

The fabrication process of the actuator is depicted in Supplementary Fig. 1a. Briefly, a SMA spring (BioMetal, BMX150) was cut into the length of ~5.3 mm and connected to sheath-stripped electric wires at both ends. The spring was then stretched to ~150% of its initial length and held in a 3D printed mold. The precursors of elastomers (Ecoflex and

Dragon skin, Smooth-On) were mixed at 1:1 ratio and poured into the mold. After 4 hours, the elastomer with SMA spring and wires was removed from the mold, thoroughly cleaned with methanol, ethanol and deionized water, and completely dried. Finally, preparation of the actuator was completed by trimming the edges and wires. The size of the actuator can be simply scaled to any dimension, but unless otherwise noted, 8 mm (length) × 1.5 mm (height) × 2 mm (width) was mainly used for this study. For animal studies, stripped electric wires were covered with elastomer, or electric wires sheathed with enamel were used to prevent any electric leakage.

The wireless, remote-controllable soft actuator was also fabricated in a manner similar to that described above, except that no electric wires were connected to the spring. To increase the area exposed to the laser, SMA springs with a wire size of 500 μm (Nitinol Micro-Springs, Kellogs Research Labs) were used.

Actuation principle

To electrically operate the actuator, the actuator was connected to an electric power supply (1403, Global specialties), a circuit board and a microprocessor (Metro 328, Adafruit) that generates electric signals to control the frequency and duty cycle of actuation. The electric circuit is depicted in Supplementary Fig. 1c. The microprocessor transmits the programmed electric signal to the electric power supply through the circuit board, and accordingly the power supply applies a voltage to the actuator to trigger its actuation.

To trigger actuation remotely, a laser of 854 nm wavelength (LD852-SE600, Thorlabs) equipped with adjustable collimator lens (LTN330-A, Thorlabs) was used. A current of 600 mA was applied to the laser to produce the maximum intensity. The laser was focused at a distance of 5 cm. The laser intensity with distance was calculated as the total laser intensity divided by the area of laser spot. The total laser intensity was measured using an optical power meter (PM160, Thorlabs), and the laser spot area was visualized using a VIS/IR detector card (VRC2, Thorlabs).

Measurements for actuation strain and force transmission

To measure the actuation strain, the soft actuators with varying stiffness were connected to an electric power supply (1403, Global specialties) to apply voltage. The actuation of soft actuators was video-recorded and post-processed using Image J and Tracker. The actuation strain was calculated as the ratio of the change in the length of SMA spring to the initial length.

Force transmission of soft actuators was measured using the Bose Test Bench LM1 system. The experimental setup was depicted in Supplementary Fig. 2b. Briefly, each end of soft actuators (1-2 mm) was glued to a rigid substrate (e.g., glass slides) and fixed to the load cell of the Bose system. The actuators were then connected to the electric power supply, and force was recorded during actuation.

Thermal measurements

Thermal measurements were performed using a thermal imaging camera (C2, FlIR). The camera was placed and focused ~15 cm away from the actuator. The thermal data was recorded and analyzed with the software (FLIR Tools plus). Lines were drawn either along the axis across the center or along the edge of actuator, and then temperature was measured along those lines. To investigate thermal responses to different frequencies, cyclic actuation was performed with varying frequencies, and the temperature along the edge of actuator was measured and reported as an averaged value. To examine the effect of the surrounding temperature, a chamber filled with distilled water was used and heated to 37 °C to provide a physiologically relevant temperature. It should be noted that the actuator was half immersed in the water, since near-infrared rays cannot penetrate water. Thermal responses to different actuation frequencies were recorded, and the temperature along the edge of actuator was averaged. Thermal imaging of the remotely controlled actuator was also conducted similarly to that described above.

Mechanical measurements

The mechanical properties of muscle tissues, elastomers and hydrogels were characterized with unconfined compression using a Bose Test Bench LM1 system following the previous method with minor modifications. Elastomer samples were prepared with a dimension of 1 ×1 × 2 cm^3 and compressed with a deformation rate of ~ 0.1 $mmsec^{-1}$. To determine the elastic modulus, the results of mechanical tests were post-processed with the assumption of hyperelasticity with incompressible neo-Hookean model (Supplementary Note 1). For the mechanical properties of muscle tissues, muscle tissues were isolated immediately after euthanization, and mechanical tests were carried out. The slope of the obtained stress-strain curve up to a strain of 5 to 15% was measured as the elastic modulus of muscle tissue.

For hydrogels, cyclic tests were performed to determine their mechanical properties under multiple compressive loads. Hydrogels were first immersed in DMEM containing physiological calcium levels (2.5 mM) for 24 hours and then subjected to 500 cyclic tests with a deformation rate of 0.9 $mmsec^{-1}$. The elastic modulus for each cycle was measured as the slope of the stress-strain curve at a strain of 5%. It should be noted that the hydrogels were surrounded by the DMEM containing 2.5 mM calcium during the testing to prevent their dehydration.

Computational simulations

Computational simulations were performed using Abaqus 6.14 (Dassault Systèmes) to determine the optimal combination of mechanical parameters of elastomers and hydrogels. The detailed description was included in the Supplementary Note 2. Briefly, a 2D finite element model was used with the assumption of plane stress. First, a simulation model for the actuator was designed with a rectangular with length and height of 80 and 15 [in arbitrary units (A.U.)], representing the elastomer body, and two squares with length of 1 [in arbitrary units (A.U.)], which represents the ends of SMA spring (Supplementary Fig. 4a). For the stiffness of elastomers, hyperelasticity with neo-Hookean model was used with the assumption of incompressibility. To generate actuation, strains were imposed on the spring ends (i.e., the squares). Given that the actuators were operated at the same voltage

in the experiment, the total strain energy in the simulation was first kept the same for all stiffnesses. The strain energy was determined as a value that closely matched the simulated strains and the experimental strains. With this strain energy, the simulation strains generally matched the experimental data, except for the lowest actuator stiffness. This soft elastomer could not maintain a tight bond with SMA due to the low polymer density, and was observed to slip during actuation in the experiment. Therefore, for this stiffness, the strain energy was adjusted to match the simulation strain and the experimental strain. The resulting strain energies were used in subsequent simulations to predict tissue deformation.

For tissue deformation simulations, a simulation model combining the actuator model described above, a tough adhesive model with length of 80 [in arbitrary units (A.U.)] and varied height, a tissue model with length and height of 160 and 40 [in arbitrary units (A.U.)] was constructed with assumption of no slip and friction between the interfaces. Strains that generated the strain energies obtained above were imposed, and tissue deformation was evaluated based on the maximum displacement divided by the initial length of the elastomer. The effect of elastomer stiffness, adhesive stiffness, adhesive thickness and tissue stiffness on tissue deformation was tested.

Bonding hydrogels on elastomers

Tough hydrogels were bonded to the elastomer component of the actuator following a previously established method[23]. Briefly, the surface of the elastomer was treated by absorbing benzophenone. Prior to treatment, the surface was thoroughly cleaned with methanol and deionized water, and dried. Benzophenone solution (10 wt% in ethanol) was then applied onto the actuator by covering the entire surface for 5 minutes at room temperature. The actuator was washed 2-3 times with methanol and completely dried. Tough hydrogels were prepared by mixing an aqueous pre-gel solution (12% acrylamide, 2% sodium alginate (LF20/40 and 5 Mrad at 1:1 ratio), 0.037% MBAA, 0.2% Irgacure 2959) with ionic crosslinker (35 mM calcium sulfate). We note that for in vivo application, ultrapure alginates (MVG and VLVG, Pronova) were used. The mixture was then quickly poured into a glass mold with a spacing of 170 μm, and kept for 30 minutes to allow the formation of ionically crosslinked network. The hydrogels were then gently removed from the mold and assembled with benzophenone-treated elastomer followed by UV irradiation (UVP Blak-Ray, 100W) for 20-30 minutes to crosslink the polyacrylamide network and to form bonds on the elastomer surface.

T-Peeling tests

The adhesion performance was quantified as the adhesion energy, the amount of interfacial energy required to propagate a unit area of interfacial crack. The adhesion energy was measured by T-peeling tests. Samples of the elastomer-hydrogel or hydrogel-tissue interface were prepared by placing and attaching a hydrogel between two elastomers or a tissue between two hydrogels. The back side of the elastomers or hydrogels were bonded to a rigid, non-stretching film (e.g., polyethylene terephthalate (PET)) with Krazy glue to prevent its stretching along the peeling direction, ensuring that all the work done by the mechanical tester was used for the energy dissipated at the crack tip. The free ends of the elastomers or hydrogels were fixed to the grips of the machine. Unidirectional tension was applied with

an Instron (3342, load cell of 50N) while recording the force and the extension. The loading rate was kept constant at 50 mm/min. The adhesion energy was determined as twice the plateau force divided by the width of the sample.

MAGENTA implantation

MAGENTA application was performed based on the previously described method[20,51] by adding an adhesive polymer (i.e., chitosan) onto the tough hydrogel of actuator-hydrogel hybrid and then adhering it to the muscle tissue. Briefly, 4% ultrapure chitosan (54046, Heppe Medical Chitosan) and coupling reagents (24 mg/mL of 1-ethyl-3-(3-dimethylaminopropyl) carbodiimide and N-hydroxysulfosuccinimide) were mixed at 1:1 ratio by vortexing. The mixture was then quickly applied to the surface of the tough hydrogel, and the applied MAGENTA was gently compressed for 5 minutes to achieve tissue adhesion.

For in vivo MAGENTA implantation, the skin around lateral gastrocnemius was incised, and the skin was gently separated from the muscle to create a space for MAGENTA implantation. A small hole was made on the opposite side of the incised skin to create a path for one electric wire of MAGENTA to exit. One of the electric wires of MAGENTA was first inserted to the hole, and adhesive polymer was deposited on the tough gel of MAGENTA as described above. The MAGENTA was then implanted onto the muscle and the skin covering the MAGENTA was gently compressed for 5 minutes. The incision was sutured using 5-0 Ethicon sutures. The procedure of the in vivo implantation of MAGENTA was depicted in the Supplementary Fig. 8. Elizabethan collars were affixed around the mice to prevent chewing of the electric wires.

Estimation of tissue deformation

To estimate tissue deformation by the actuation of MAGENTA, amputated mouse hindlimbs were used as ex vivo models. To visualize tissue deformation, acrylic paints (Sargent Art) were sprayed onto the hindlimbs, and MAGENTA was applied following the procedure as described above. The MAGENTA was then connected to the electric power supply and the microprocessor, and a voltage of 6V was applied to generate actuation. The displacement of the paint speckles was recorded with a digital camera, and analyzed using a speckle tracking method[52] (Ncorr: 2D-Digital image correlation). The displacement fields were created by comparing the images of the hindlimbs before and after the actuation. The areas with electric wires were excluded from the analysis.

Muscle atrophy model and mechanical stimulation

To induce muscle atrophy, hindlimb immobilization was performed in female C57BL6/J mice at 14-18 weeks of age (Jackson Laboratory) following the previously established method with some modifications[53]. The hindlimb was first shaved prior to immobilization, and on the day of immobilization, animals were anesthetized using isoflurane inhalation. One hindlimb was maintained in a knee joint extension and ankle plantar flexion position, and fixed by wrapping with the non-elastic surgical bandages (Micropore surgical tape and Transpore surgical tape, 3M) to the foot. The forefoot portion was left exposed to monitor adverse events. This surgical taping was maintained for either 2 weeks or 3 weeks

depending on the experimental setting. Since hindlimb immobilization was performed on only one hindlimb, the other limb allowed the animal to remain ambulatory. All animal procedures were performed in accordance with the Harvard University Faculty of Arts and Sciences Institutional Animal Care and Use Committee guidelines. Mice were kept at a 12 hours light/12 hours night cycle, at a temperature of 20-24 °C and humidity of 35-65 %. For mechanical stimulation, mice were anesthetized with isoflurane during mechanical stimulation, and untreated mice were also placed in the isoflurane chamber to keep the amount of exposure to the anesthetic agent the same for the groups. In the prevention experiments where both immobilization and stimulation were performed in the same timeline, the surgical tapes were gently removed from the hindlimb, and an electric power supply (1403, Global specialties) was connected to the MAGENTA. The voltage that produced the maximum actuation strain was applied (~6 V). Actuation frequency was selected to the maximum value at which the temperature of MAGENTA does not exceed the physiological range (0.1 Hz, and duty cycle of 4% on and 96% off). On the basis of previous in vitro studies[54-56] showing that 3-5 minutes of stretching improved the muscle functions of engineered skeletal muscle tissues, mechanical stimulation of 5 minutes was performed every day. The hindlimb bandages were also removed from the untreated mice for the same amount of time each day to maintain the same condition as the treated mice. In the stimulation-discontinuation experiment, stimulation was given only in the first week of the 2-week study. In the recovery test, the bandages were already removed at the time of stimulation, therefore mechanical stimulation was performed under the same conditions as the prevention experiments except for the bandage removal step.

Ultrasound imaging

For ultrasound imaging, MAGENTA-implanted animals were anesthetized, placed on a heating pad, and the hindlimbs were fixed to prevent movement. Muscles were analyzed with photoacoustic imaging using a Vevo 770 scanner with a 35 MHz transducer (VisualSonics, axial resolution: 50μm, lateral resolution, 140μm). The scanner was placed directly above where the MAGENTA was located. During ultrasound imaging in the sagittal plane, voltage was applied to the MAGENTA to enable its actuation. After imaging, animals were subsequently allowed to recover to their normal behavior. Images captured were analyzed to estimate muscle displacement driven by the actuation of MAGENTA. Kymographs were created using ImageJ with a stack of ultrasound images at different time points. A line was drawn across a noticeable tissue signal along the MAGENTA axis. Image pixels that the line passed through were then reorganized to create a kymograph.

Muscle function analysis

The muscle function of isolated lateral gastrocnemius and tibialis anterior muscles was measured as previously described[12,15]. Briefly, explanted muscles were placed between two steel electrodes (1.6 mm diameter, 21 mm long) and fixed with micro-clippers at both ends. The upper of the two clippers was connected to a force transducer (FORT 25, WPII). During muscle function tests, the muscles were bathed in a physiologic saline solution chamber continuously supplied with oxygen at 37°C. Electric stimulation of the muscles and data acquisition were performed through LabVIEW (2019, National Instruments). A wave pulse was initiated and delivered to the electrodes via power amplifier (QSC USA 1310). Tetanic

contraction was evoked at 30, 35, and 40V with frequencies of 10 Hz/V. A constant pulse width of 2 milliseconds and a train duration of 1 second were used. The muscles were rested for 5 minutes between the stimulations. To remove the noise and select appropriate value, a 10^{th} order one dimensional median filter was used. Maximum tetanic force was defined as the difference between the maximum force during stimulation and the baseline. Each muscle weight was used for normalization.

Histology and immunofluorescence analysis

For histological analysis, isolated muscles were fixed in 4% paraformaldehyde, washed, paraffin-embedded and stained with Hematoxylin & Eosin (H&E) or Masson's Trichrome. The sections were imaged with Nikon E800 in a bright field mode.

Immunohistochemistry was performed for both paraffin sections and cryostat sections. Paraffin sections were first deparaffinized, and then processed with antigen retrieval treatments using Dako Target Retrieval Solution (Agilent) and Proteinase K (Thermo Fischer Scientific), prior to standard immunostaining procedures. For cryostat sections, isolated muscles were fixed in 4% paraformaldehyde, washed, incubated in 30% sucrose at 4°C overnight, and placed in a 50:50 mixture of 30% sucrose solution and O.C.T. (Tissue-Tek) for another overnight. The mix solution was removed, and the tissues were then embedded in O.C.T., frozen, and sectioned with a thickness of 20-40 μm using a cryostat (Leica Biosystems). The sectioned samples were stained using standard immunohistochemistry protocols. The samples were permeabilized with PBS containing 0.1% Tween 20 or Triton X (PBST), blocked with PBST containing 10% bovine serum albumin and 10% goat serum. The following antibodies and reagents were used for immunohistochemistry: laminin antibody (1:100, ab11575, Abcam), MRTFA (1:100, PA5-109960, Thermo Fisher Scientific), YAP (1:100, ab205270, Abcam), Pax7 (1:100, ab187339, Abcam), Ki67 (1:100, ab15580, Abcam), MHC (1:100, MAB4470, R&D systems), Desmin (1:100, ab15200, Abcam), CD31 (1:100, ab124432, Abcam), Prolong Gold antifade reagent (Invitrogen) and DAPI (Invitrogen).

Image analysis

To quantify muscle fiber size, images of laminin-stained muscle tissues were obtained with a laser scanning confocal microscope with ×10/×20 objective (Zeiss, LSM710). The cross-sectional area of muscle fibers was then estimated using Image J with a plug-in MorphoLibj. To analyze cells positive for YAP, MRTFA, Ki67, and Pax7, images were taken using a laser scanning confocal microscope with ×20 objective (Zeiss, LSM710), and thresholded in each channel to identify the location of the protein of interest and nuclear area. The fraction of cells positive for the protein of interest was quantified as the number of cells exhibiting nuclear localization divided by the total number of cells.

The blue intensity of Masson's Trichrome staining, indicative of matrix protein, particularly collagen, was assessed using ImageJ. Images were first processed through color deconvolution and then thresholded with RenyiEntrophy. A histogram of intensity was collected, and the mean value was determined for each image.

For spatial reconstruction of YAP and MRTFA staining, tile scanning (Zeiss, LSM710) was performed to capture the entire longitudinal section of the muscle. Regions of interest (ROIs) of 500 μm × 500 μm square were randomly selected throughout the section, and the fractions of cells positive for YAP and MRTFA were measured. Tissue depth was defined as the horizontal distance between the center of the ROI and the edge of the muscle section on the stimulation side.

Protein extraction and immunoblot

Isolated skeletal muscles were lysed in tissue protein extraction buffer (78510, Thermo Fisher Scientific) supplemented with phosphatase inhibitors cocktail (1861281, Thermo Fisher Scientific) and 0.1 mg/ml of phenylmethylsulphonyl fluoride. Protein concentrations were quantified using Pierce Bicinchoninic Acid Protein Assay Kit (23227, Thermo Fisher Scientific) as per the manufacturer's instructions. Laemmli sample buffer (1610747, Bio-Rad) was added to lysates, and samples were boiled for 10 minutes before loading in a polyacrylamide gradient gel (4561086, Bio-Rad). Proteins were separated and transferred to nitrocellulose at 100V for 1 hour, blocked with 4% non-fat milk in TBS-T, incubated overnight with primary antibodies followed by incubation for 1 hour at RT with horseradish peroxidase-conjugated secondary antibodies and detection using enhanced chemiluminescent detection reagent (34577, Thermo Fisher Scientific). The following primary antibodies were used for immunoblotting; YAP antibody (1:1000, ab205270, Abcam), MRTFA antibody (1:1000, PA5-109960, Thermo Fisher Scientific), MuRF1 (1:500, sc-398608, Santa Cruz), Akt (1:500, 4685S, Cell Signaling Technology), phospho-Akt (1:500, 4060T, Cell Signaling Technology), GAPDH (1:1000, ab9485, Abcam), and puromycin antibody (1:2500, 12D10, Millipore,). Secondary antibodies used were goat anti-mouse IgG2a conformation specific antibody (1:5000, 115-035-206, Jackson Immuno Research) for puromycin, goat anti-mouse for MuRF1 (1:5000, 405306, BioLegend), and donkey anti-rabbit (1:5000, 406401, BioLegend) for the rest of proteins. Densitometry was performed using ImageJ, and the protein levels were normalized to those of GAPDH. Uncropped scans of western blots are provided in the Source Data files and Supplementary files.

In vivo estimation of protein synthesis

Protein synthesis was analyzed using SuNSET[57]. Briefly, the mice were injected with 0.04 μmol/g^{-1} body weight of puromycin (P8833, Sigma) dissolved in PBS through an intraperitoneal injection. At 30 minutes after injection, muscles were collected. The tissues were processed as described above for protein extraction and immunoblot. To control for variation in sample loading, samples were loaded twice; one lane for puromycin and the other lane for GADPH normalization.

Ex vivo implantation depth analysis

The responsiveness of wireless MAGENTA versus tissue implantation depth was assessed through ex vivo experiments. To mimic various depths of tissue, 1 mm and 1.5 mm thick porcine skin and 2 mm thick mouse muscle tissue were prepared. The wireless version of MAGENTA was applied to the amputated hindlimb muscles, and then the prepared skin and muscle tissues were placed on top to fully cover the MAGENTA. The laser, which

was mounted on a positioning device consisting of a stand and clamp, was placed over the tissue-covered MAGENTA. The laser was then turned on, and the actuation of MAGENTA was video-recorded.

Supplementary Material

Refer to Web version on PubMed Central for supplementary material.

Acknowledgements

This work was supported by the National Institute of Dental & Craniofacial Research (R01DE013349), the Eunice Kennedy Shriver National Institute of Child Health & Human Development (P2CHD086843), and the National Science Foundation MRSEC at Harvard University (DMR14-20570). S.N. gratefully acknowledges funding support from the Wyss Technology Development Fellowship. A.J.N. acknowledges a Graduate Research Fellowship from the National Science Foundation. S.L.M. acknowledges funding support from the National Institute of Arthritis and Musculoskeletal and Skin Diseases (F31AR075367). Additionally, the authors thank Mooney laboratory members for helpful discussions. We thank Dana-Farber/Harvard Cancer Center in Boston, MA, for the use of the Rodent Histopathology Core.

Data availability

Data supporting the findings of this study are available in the article and its supplementary files, and deposited at https://doi.org/10.7910/DVN/C3G80C. Unprocessed western blots are provided in Source Data files and Supplementary files. Source data are provided with this paper.

Code availability

The custom code for controlling the actuation of MAGENTA is available at https://github.com/sungminnam/MAGENTAcode/blob/main/MAGENTA.

References

1. DuFort CC, Paszek MJ & Weaver VM Balancing forces: architectural control of mechanotransduction. Nat. Rev. Mol. Cell Biol 12, 308–319 (2011). [PubMed: 21508987]
2. Vogel V & Sheetz M Local force and geometry sensing regulate cell functions. Nat. Rev. Mol. Cell Biol 7, 265–275 (2006). [PubMed: 16607289]
3. Powell CA, Smiley BL, Mills J & Vandenburgh HH Mechanical stimulation improves tissue-engineered human skeletal muscle. Am. J. Physiol. - Cell Physiol 283, 1557–1565 (2002).
4. Gudipaty SA et al. Mechanical stretch triggers rapid epithelial cell division through Piezo1. Nature 543, 118–121 (2017). [PubMed: 28199303]
5. Benham-Pyle BW, Pruitt BL & Nelson WJ Mechanical strain induces E-cadherin-dependent Yap1 and β-catenin activation to drive cell cycle entry. Science 348, 1024–1027 (2015). [PubMed: 26023140]
6. Moon DG, Christ G, Stitzel JD, Atala A & Yoo JJ Cyclic mechanical preconditioning improves engineered muscle contraction. Tissue Eng. - Part A 14, 473–482 (2008). [PubMed: 18399787]
7. Rangarajan S, Madden L & Bursac N Use of flow, electrical, and mechanical stimulation to promote engineering of striated muscles. Ann. Biomed. Eng 42, 1391–1405 (2014). [PubMed: 24366526]
8. Du V. et al. A 3D magnetic tissue stretcher for remote mechanical control of embryonic stem cell differentiation. Nat. Commun 8, (2017).
9. Chin M & Toth BA Distraction osteogenesis in maxillofacial surgery using internal devices: Review of five cases. J. Oral Maxillofac. Surg 54, 45–53 (1996). [PubMed: 8530999]

10. Aragona M. et al. Mechanisms of stretch-mediated skin expansion at single-cell resolution. Nature 584, 268–273 (2020). [PubMed: 32728211]
11. Iliadi A, Koletsi D & Eliades T Forces and moments generated by aligner-type appliances for orthodontic tooth movement: A systematic review and meta-analysis. Orthod. Craniofac. Res 22, 248–258 (2019). [PubMed: 31237410]
12. Cezar CA et al. Biologic-free mechanically induced muscle regeneration. Proc. Natl. Acad. Sci. U. S. A 113, 1534–1539 (2016). [PubMed: 26811474]
13. Miller BF et al. Enhanced skeletal muscle regrowth and remodelling in massaged and contralateral non-massaged hindlimb. J. Physiol 596, 83–103 (2018). [PubMed: 29090454]
14. Crane JD et al. Massage therapy attenuates inflammatory signaling after exercise-induced muscle damage. Sci. Transl. Med 4, 119ra13 (2012).
15. Seo BR et al. Skeletal muscle regeneration with robotic actuation–mediated clearance of neutrophils. Sci. Transl. Med 13, eabe8868 (2021). [PubMed: 34613813]
16. Lendlein A & Gould OEC Reprogrammable recovery and actuation behaviour of shape-memory polymers. Nat. Rev. Mater 4, 116–133 (2019).
17. Laschi C, Mazzolai B & Cianchetti M Soft robotics: Technologies and systems pushing the boundaries of robot abilities. Sci. Robot 1, 1–12 (2016).
18. Jani JM, Leary M, Subic A & Gibson MA A review of shape memory alloy research, applications and opportunities. Mater. Des 56, 1078–1113 (2014).
19. Huang X. et al. Shape memory materials for electrically-powered soft machines. J. Mater. Chem. B 8, 4539–4551 (2020). [PubMed: 32373836]
20. Li J. et al. Tough adhesives for diverse wet surfaces. Science 357, 378–381 (2017). [PubMed: 28751604]
21. Nam S & Mooney D Polymeric Tissue Adhesives. Chem. Rev (2021).
22. Yuk H, Zhang T, Lin S, Parada GA & Zhao X Tough bonding of hydrogels to diverse non-porous surfaces. Nat. Mater 15, 190–196 (2016). [PubMed: 26552058]
23. Yuk H, Zhang T, Parada GA, Liu X & Zhao X Skin-inspired hydrogel-elastomer hybrids with robust interfaces and functional microstructures. Nat. Commun 7, 12028 (2016). [PubMed: 27345380]
24. Cohen S, Nathan JA & Goldberg AL Muscle wasting in disease: Molecular mechanisms and promising therapies. Nat. Rev. Drug Discov 14, 58–74 (2015). [PubMed: 25549588]
25. Gao Y, Arfat Y, Wang H & Goswami N Muscle atrophy induced by mechanical unloading: Mechanisms and potential countermeasures. Front. Physiol 9, (2018).
26. Sartori R, Romanello V & Sandri M Mechanisms of muscle atrophy and hypertrophy: implications in health and disease. Nat. Commun 12, 1–12 (2021). [PubMed: 33397941]
27. Jones SW et al. Disuse atrophy and exercise rehabilitation in humans profoundly affects the expression of genes associated with the regulation of skeletal muscle mass. FASEB J. 18, 1025–1027 (2004). [PubMed: 15084522]
28. Tyganov SA et al. Effects of plantar mechanical stimulation on anabolic and catabolic signaling in rat postural muscle under short-term simulated gravitational unloading. Front. Physiol 10, 1252 (2019). [PubMed: 31611819]
29. Moya IM & Halder G Hippo–YAP/TAZ signalling in organ regeneration and regenerative medicine. Nat. Rev. Mol. Cell Biol 20, 211–226 (2019). [PubMed: 30546055]
30. Totaro A, Panciera T & Piccolo S YAP/TAZ upstream signals and downstream responses. Nat. Cell Biol 20, (2018).
31. Bodine SC et al. Identification of ubiquitin ligases required for skeletal Muscle Atrophy. Science 294, 1704–1708 (2001). [PubMed: 11679633]
32. Bodine SC et al. Akt/mTOR pathway is a crucial regulator of skeletal muscle hypertrophy and can prevent muscle atrophy in vivo. Nat. Cell Biol 3, 1014–1019 (2001). [PubMed: 11715023]
33. Barclay RD, Burd NA, Tyler C, Tillin NA & Mackenzie RW The Role of the IGF-1 Signaling Cascade in Muscle Protein Synthesis and Anabolic Resistance in Aging Skeletal Muscle. Front. Nutr 6, 146 (2019). [PubMed: 31552262]

34. Stitt TN et al. The IGF-1/PI3K/Akt pathway prevents expression of muscle atrophy-induced ubiquitin ligases by inhibiting FOXO transcription factors. Mol. Cell 14, 395–403 (2004). [PubMed: 15125842]
35. Jacques SL Optical properties of biological tissues: A review. Phys. Med. Biol 58, R37–R61 (2013). [PubMed: 23666068]
36. Gonçalves AI et al. Exploring the Potential of Starch/Polycaprolactone Aligned Magnetic Responsive Scaffolds for Tendon Regeneration. Adv. Healthc. Mater 5, 213–222 (2016). [PubMed: 26606262]
37. Li Y, Guo M & Li Y Recent advances in plasticized PVC gels for soft actuators and devices: A review. J. Mater. Chem. C 7, 12991–13009 (2019).
38. Waters-Banker C, Butterfield TA & Dupont-Versteegden EE Immunomodulatory effects of massage on nonperturbed skeletal muscle in rats. J. Appl. Physiol 116, 164–175 (2014). [PubMed: 24201707]
39. Roche ET et al. Soft robotic sleeve supports heart function. Sci. Transl. Med 9, eaaf3925 (2017). [PubMed: 28100834]
40. Zhu M, Do TN, Hawkes E & Visell Y Fluidic Fabric Muscle Sheets for Wearable and Soft Robotics. Soft Robot. 7, 2 (2020).
41. Polygerinos P, Wang Z, Galloway KC, Wood RJ & Walsh CJ Soft robotic glove for combined assistance and at-home rehabilitation. Rob. Auton. Syst 73, 135–143 (2015).
42. Chu SY et al. Mechanical stretch induces hair regeneration through the alternative activation of macrophages. Nat. Commun 10, 1524 (2019). [PubMed: 30944305]
43. He Q. et al. Electrically controlled liquid crystal elastomer-based soft tubular actuator with multimodal actuation. Sci. Adv 5, eaax5746 (2019). [PubMed: 31646178]
44. Kotikian A, Truby RL, Boley JW, White TJ & Lewis JA 3D Printing of Liquid Crystal Elastomeric Actuators with Spatially Programed Nematic Order. Adv. Mater 30, 1–6 (2018).
45. Xie W, Ouyang R, Wang H, Li N & Zhou C Synthesis and cytotoxicity of novel elastomers based on cholesteric liquid crystals. Liq. Cryst 47, 449–464 (2020).
46. Lin R. et al. Wireless battery-free body sensor networks using near-field-enabled clothing. Nat. Commun 11, 1–10 (2020). [PubMed: 31911652]
47. Yamagishi K. et al. Tissue-adhesive wirelessly powered optoelectronic device for metronomic photodynamic cancer therapy. Nat. Biomed. Eng 3, 27–36 (2019). [PubMed: 30932063]
48. Chung HU et al. Binodal, wireless epidermal electronic systems with in-sensor analytics for neonatal intensive care. Science 363, eaau0780 (2019). [PubMed: 30819934]
49. Kim J, Campbell AS, de Ávila BEF & Wang J Wearable biosensors for healthcare monitoring. Nat. Biotechnol 37, 389–406 (2019). [PubMed: 30804534]
50. Chen Y. et al. Flexible inorganic bioelectronics. npj Flex. Electron 4, (2020).
51. Freedman BR et al. Enhanced tendon healing by a tough hydrogel with an adhesive side and high drug-loading capacity. Nat. Biomed. Eng (2022).
52. Blaber J, Adair B & Antoniou A Ncorr: Open-Source 2D Digital Image Correlation Matlab Software. Exp. Mech 55, 1105–1122 (2015).
53. Aihara M. et al. A new model of skeletal muscle atrophy induced by immobilization using a hook-and-loop fastener in mice. J. Phys. Ther. Sci 29, 1779–1783 (2017). [PubMed: 29184288]
54. Kim H, Kim MC & Asada HH Extracellular matrix remodelling induced by alternating electrical and mechanical stimulations increases the contraction of engineered skeletal muscle tissues. Sci. Rep 9, 2732 (2019). [PubMed: 30804393]
55. Lin SS & Liu YW Mechanical stretch induces mTOR recruitment and activation at the phosphatidic acid-enriched macropinosome in muscle cell. Front. Cell Dev. Biol 7, 78 (2019). [PubMed: 31139627]
56. Rauch C & Loughna PT Static stretch promotes MEF2A nuclear translocation and expression of neonatal myosin heavy chain in C2C12 myocytes in a calcineurin- and p38-dependent manner. Am. J. Physiol. Cell Physiol 288, 593–605 (2005).
57. Watt KI et al. The Hippo pathway effector YAP is a critical regulator of skeletal muscle fibre size. Nat. Commun 6, 6048 (2015). [PubMed: 25581281]

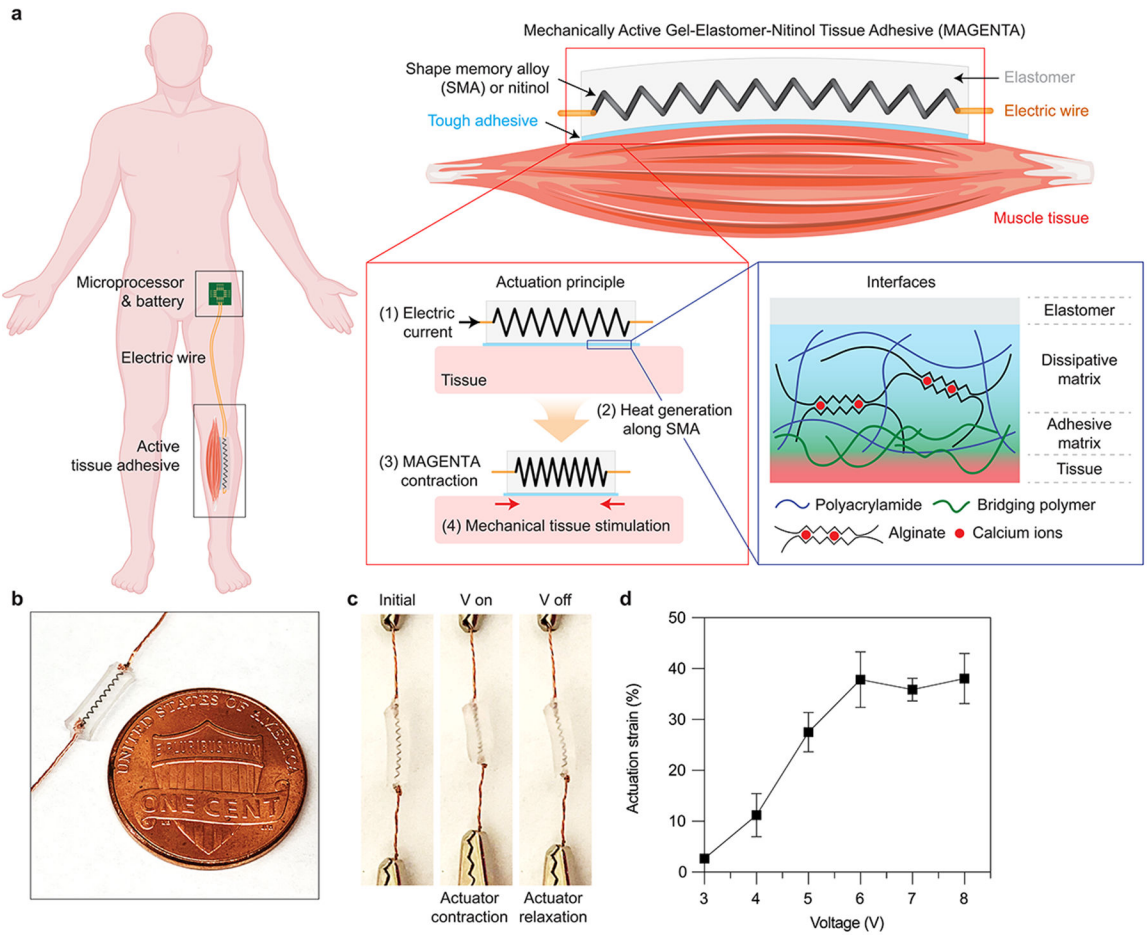

Figure 1. MAGENTA provides mechanical stimulation to the target tissue.

a, A schematic depicting the potential application of MAGENTA and its actuation principle to generate mechanical stimulation. **b,** An example of a soft actuator fabricated with a SMA spring and an elastomer. **c,** An example of contraction and relaxation of an actuator during actuation. The actuator contracted immediately upon application of voltage, and relaxed once the voltage was discontinued. **d,** Actuation strain as a function of applied voltage (n = 3, 3, 3, 6, 3, 3 actuators). Data represent mean ± SD.

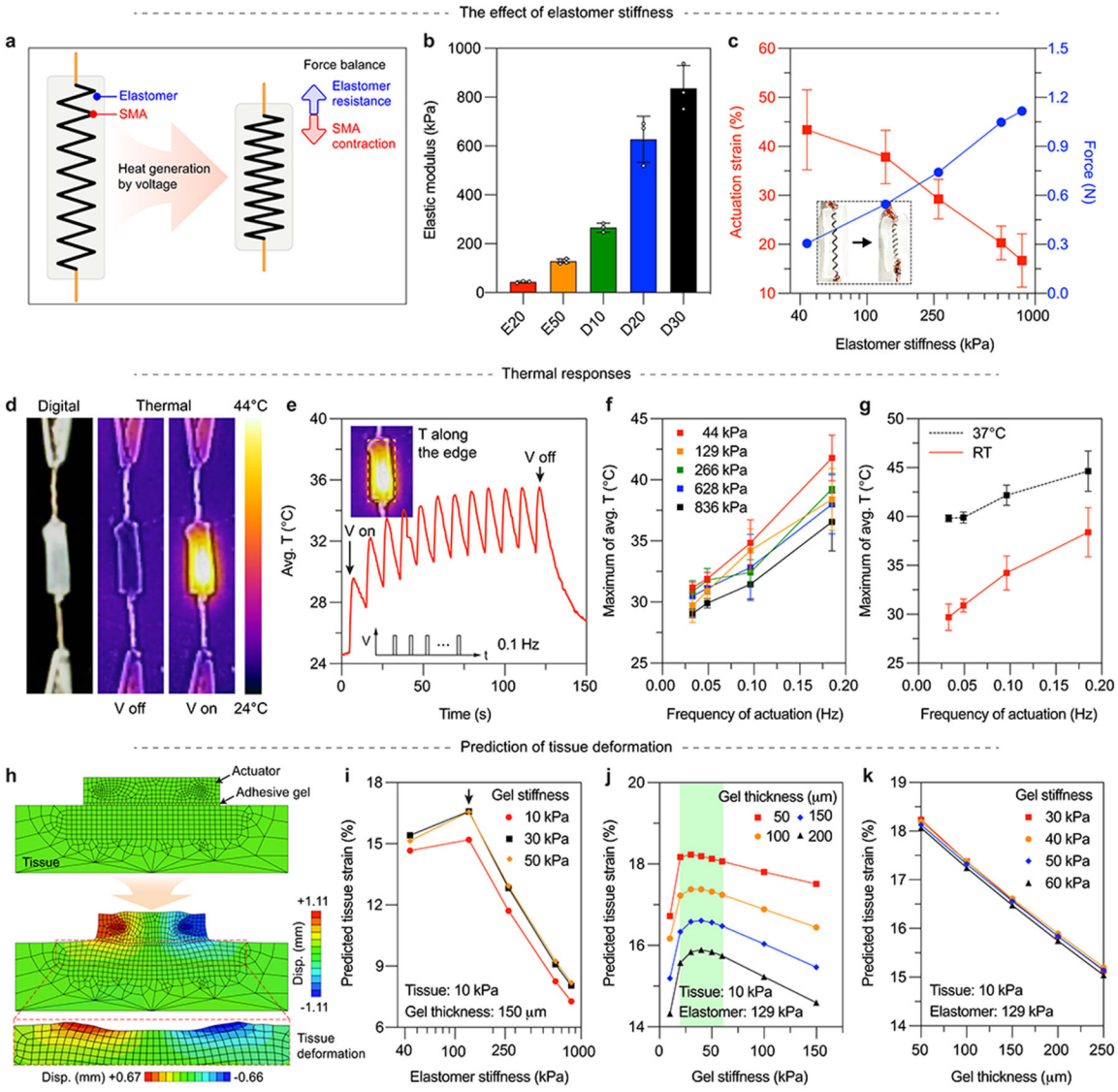

Figure 2. Mechanical and thermal performance of soft actuators and prediction of tissue deformation.

a, A schematic illustration of force balance between spring contraction and elastomer resistance during actuation. **b,** Elastic moduli of elastomers used in actuators (n = 3, 3, 4, 3, 3 elastomers). E20, E50, D10, D20 and D30 represent Ecoflex™ 00-20, 00-50, Dragon Skin™ 10, 20 and 30, respectively. **c,** Actuation strain and force transmission as a function of elastomer stiffness. Actuation strain; n = 3, 6, 3, 3, 5 actuators. Force; n = 1, 1, 1, 2, 2 actuators. **d,** Digital (left) and thermal images of an actuator before (middle) and after (right) application of voltage. **e,** Time evolution of temperature averaged along the edge of actuators during cyclic actuation. The frequency of actuation was 0.1 Hz. Each peak indicates when the voltage was applied during the cycle. The maximum of temperature averaged along the edge of actuators during cyclic actuation versus actuation frequency for **f,** various elastomer stiffnesses (44 kPa; n = 7, 7, 12, 21 peaks, 129 kPa; n = 6, 7, 12, 25 peaks, 266 kPa; n = 8, 7, 13, 22 peaks, 628 kPa; n = 5, 6, 17, 21 peaks, 836 kPa; n = 5, 6, 11, 22 peaks per

condition), and **g,** different ambient temperatures (RT; n = 6, 7, 12, 25 peaks, 37 °C; n = 6, 7, 18, 21 peaks per condition). **h,** A simulation model combining the actuator, adhesive and tissue model to predict tissue deformation. Predicted tissue deformation as a function of **i,** elastomer stiffness, **j,** adhesive gel stiffness, and **k,** adhesive gel thickness. Black arrow indicates the greatest predicted tissue strain. Data are shown as mean ± SD.

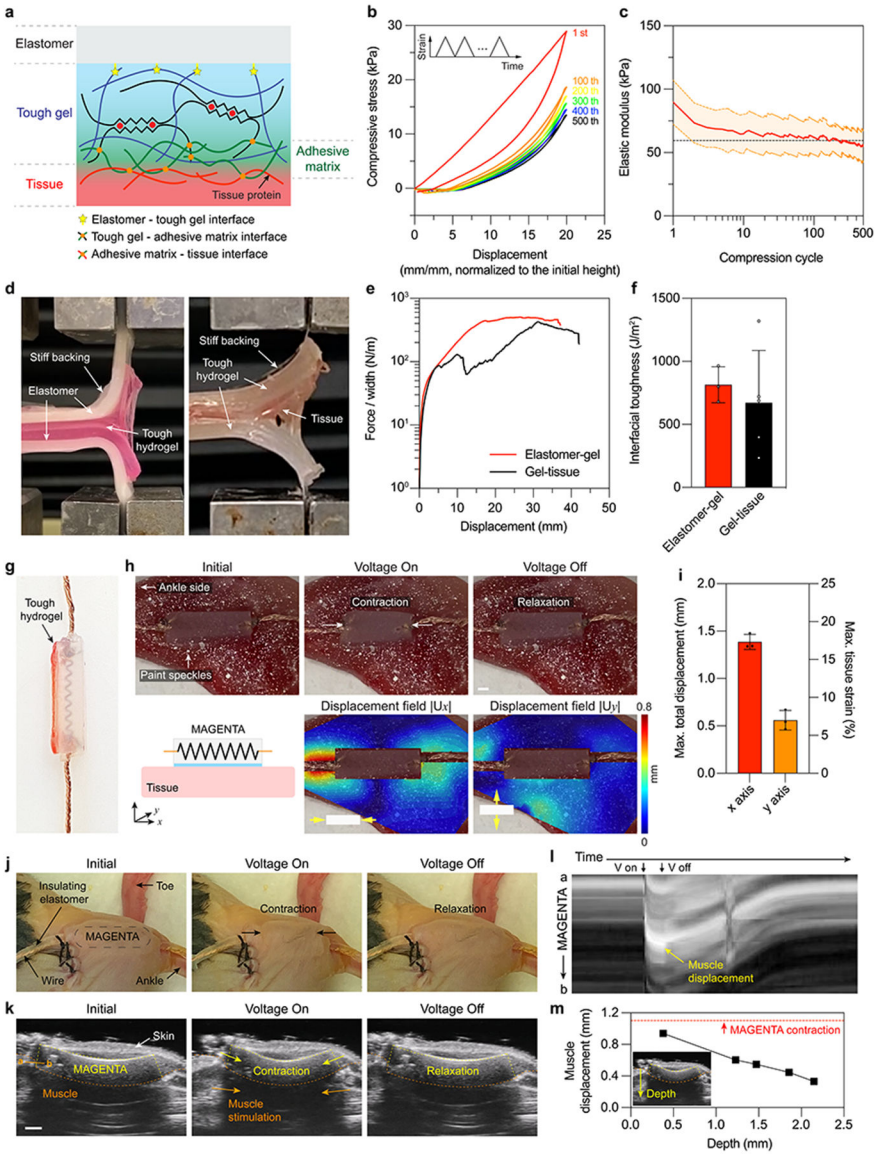

Figure 3. Ex vivo and in vivo application of MAGENTA.

a, A schematic illustration of a robust interface formation between elastomer, tough gel and tissue. **b,** Compressive stress of tough hydrogels during cyclic deformation. **c,** Elastic modulus of tough gels over cycles of deformation (n = 5 independent samples). **d,** Photos of T-peeling tests for the elastomer-hydrogel (left) and hydrogel-tissue (right) interface. **e,** Curves of the peeling force per width versus displacement for the elastomer-hydrogel and hydrogel-tissue interface. **f,** Calculated interfacial toughness (n = 3, 5 independent samples). **g,** A photo of actuator-adhesive hybrid. **h,** Ex vivo application of MAGENTA. Photos of skeletal muscle tissue deformation generated during actuation of MAGENTA (top) and corresponding displacement fields (bottom) acquired by the paint speckle tracking analysis. **i,** Estimated maximum tissue displacement and tissue strain along the actuator axis (x axis) and the perpendicular axis (y axis) (n = 3 independent samples). **j,** In vivo application of MAGENTA. Photos of skin surrounding the implanted MAGENTA during actuation.

k, Ultrasound images of tissue deformation during actuation. **l,** A kymograph of tissue displacement, based on ultrasound images, during MAGENTA actuation. The specific line tracked over time is indicated in the solid orange line (**k,** right). **m,** Estimation of muscle displacement as a function of tissue depth. Data are shown as mean ± SD. Scale bars, 1 mm.

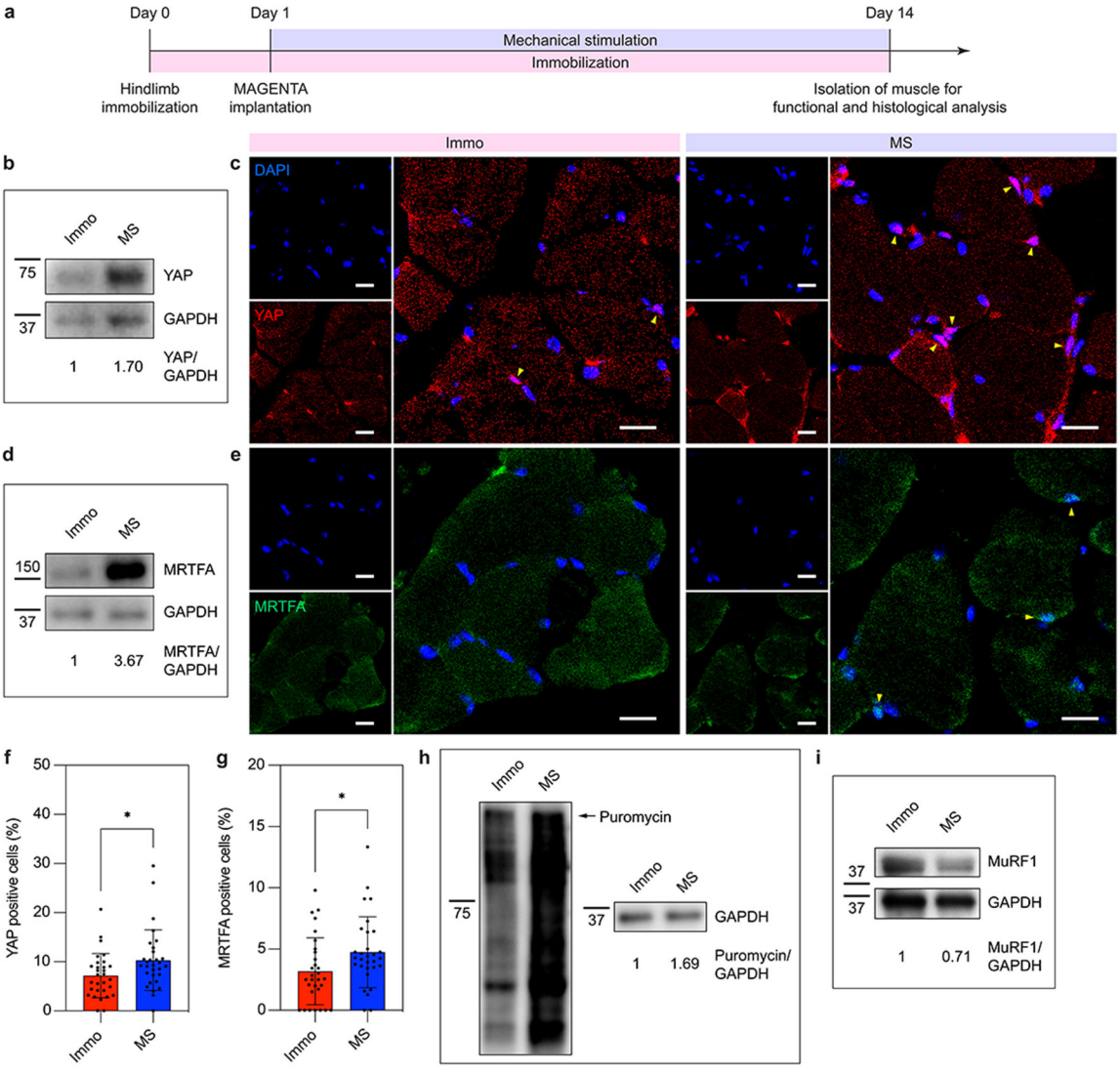

Figure 4. Mechanical stimulation by MAGENTA activates mechanosensors and increases protein synthesis in disuse muscles.

a, Experimental design and timeline of hindlimb immobilization, mechanical stimulation and analysis. **b,** Immunoblot of YAP for untreated muscles (Immo) and mechanically stimulated muscles (MS). GAPDH, glyceraldehyde-3-phosphate dehydrogenase. **c,** Fluorescence images of YAP in muscle tissues treated with and without mechanical stimulation. Yellow arrowheads indicate nuclear localized YAP. **d,** Immunoblot of MRTFA for untreated muscles (Immo) and mechanically stimulated muscles (MS). **e,** Fluorescence images of MRTFA in muscle tissues treated with and without mechanical stimulation. Yellow arrowheads indicate nuclear localized MRTFA. Fraction of cells positive for **f,** nuclear YAP or **g,** MRTFA. Immunoblots of **h,** puromycin and **i,** MuRF1 for muscles with and without mechanical stimulation. All scale bars, 20 μm. (**b**, **c**, **d**, and **e**) Tissue samples were collected from three muscles. In **f** and **g**, n = 30 images in total from 3 muscles for each group. Stimulation was performed every day for 2 weeks at the actuator's maximum strain and a frequency of 0.1 Hz for 5 min per day (420 cycles in total, duty cycle of 4% on and

96% off). Two-sided Student's t tests were used (*P < 0.05; n.s., not significant). Data are shown as mean ± SD.

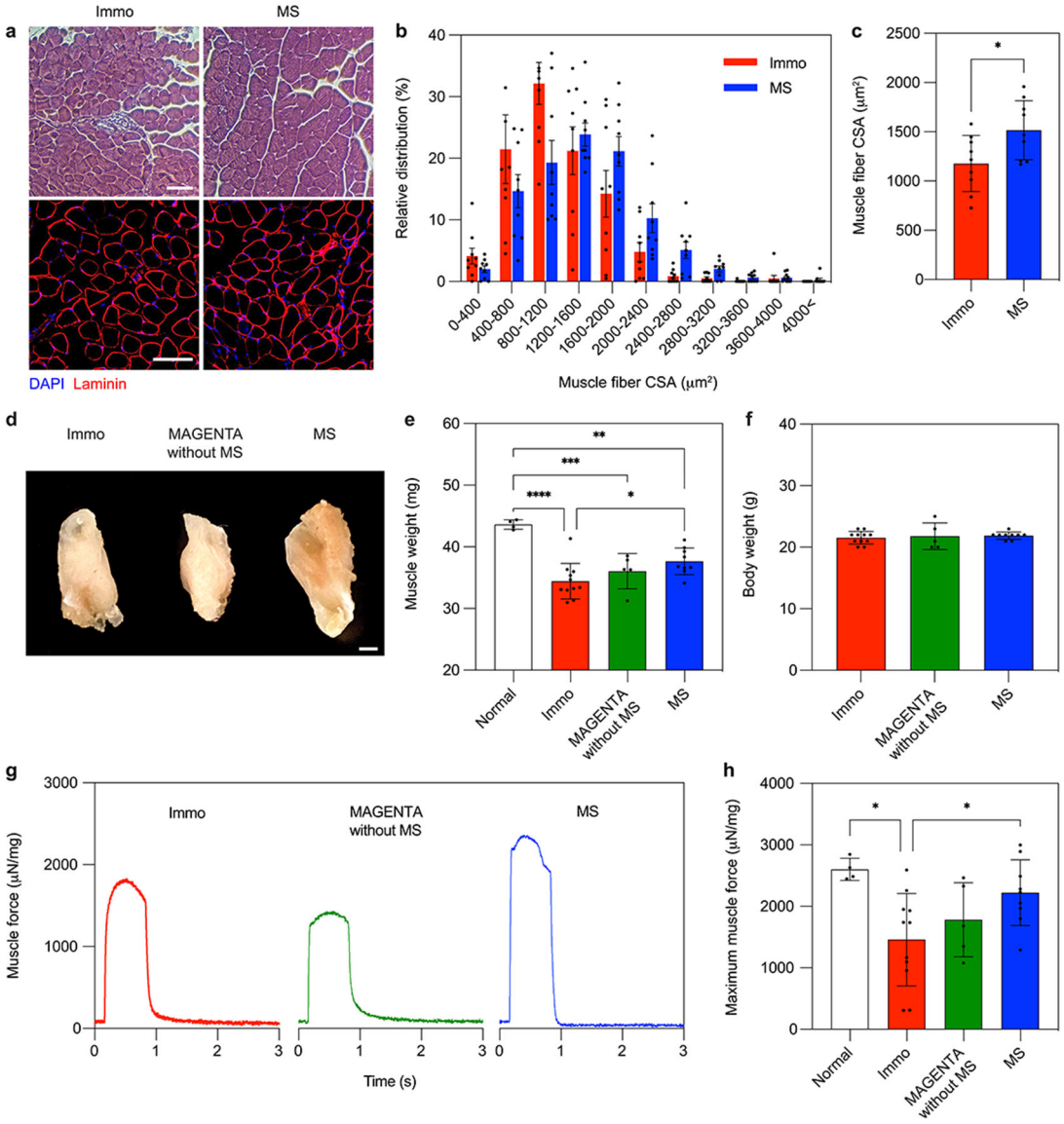

Figure 5. Mechanical stimulation by MAGENTA delays the occurrence of muscle atrophy, maintaining muscle size and weight and muscle function.

a, Representative images of muscle fibers from mice treated with or without mechanical stimulation after 2 weeks, stained with hematoxylin and eosin (H&E) (top) and laminin (bottom). Tissue sections were collected from three muscle samples. Scale bars, 100 μm. **b,** Relative distribution and **c,** quantification of cross-sectional area (CSA) of muscle fibers (n = 9 images in total from 3 muscles for each group). **d,** Photos of lateral gastrocnemius muscle tissue from untreated mice (Immo), mice implanted with MAGENTA but without mechanical stimulation (MAGENTA without MS), and mice implanted with MAGENTA and received mechanical stimulation (MS). Scale bar, 1 mm. **e,** Muscle weight of lateral gastrocnemius (n = 4, 11, 5, 9 mice). The group of mice without hindlimb immobilization is indicated as 'Normal'. **f,** Body weight of mice from each group (n = 11, 5, 9 mice). **g,** Representative muscle force normalized by the muscle weight. **h,** Measurement for maximum muscle force generation (n = 4, 11, 5, 9 mice). Stimulation was performed every

day for 2 weeks at the actuator's maximum strain and a frequency of 0.1 Hz for 5 min per day (420 cycles in total, duty cycle of 4% on and 96% off). In **b**, data are shown as mean ± SEM. In **e**, **f** and **h**, data represent mean ± SD. In **c**, Two-sided Student's t tests were used, *P < 0.05. In **e** and **h**, an ordinary one-way ANOVA with post hoc Tukey's multiple comparisons was used, *P < 0.05, **P < 0.01, ***P < 0.001, and ****P < 0.0001.

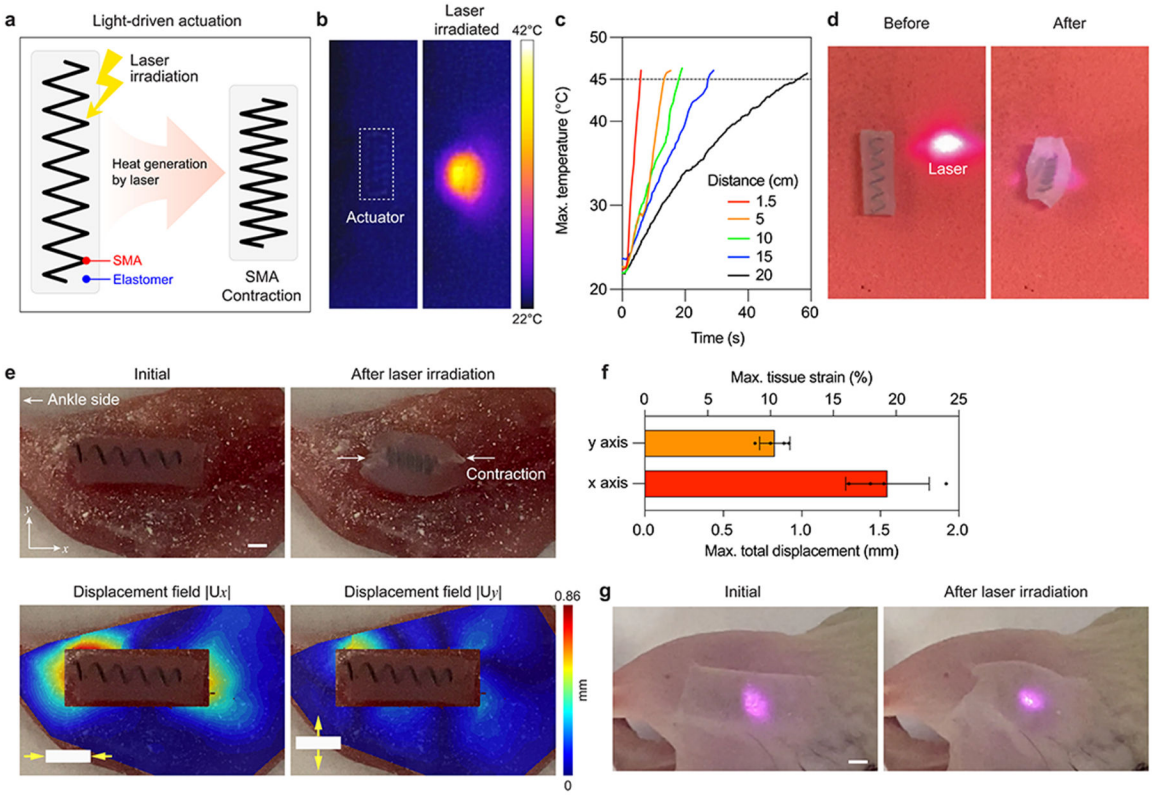

Figure 6. Wireless, remote-controllable MAGENTA with a laser.

a, A schematic illustration of the laser-triggered actuation of MAGENTA. **b,** Thermal images of wireless MAGENTA before and after laser irritation. **c,** Time evolution of maximum temperature of wireless MAGENTA in response to a laser irradiated at various distances. **d,** Actuation of wireless MAGENTA before and after laser irradiation. **e,** Ex vivo application of wireless, remote-controllable MAGENTA. Photos of tissue deformation generated during actuation of wireless MAGENTA (top) and corresponding displacement fields (bottom). **f,** Estimated maximum tissue displacement and tissue strain along the actuator axis (x axis) and the perpendicular axis (y axis) (n = 4 independent samples). **g,** In vivo application of wireless MAGENTA. Photos of the skin surrounding the implanted wireless MAGENTA before and after laser application. Data are shown as mean ± SD. Scale bars, 1 mm.